CrossMark

Influence of Zn Substitution on Structural, Magnetic and Electrical Properties of MgFe$_2$O$_4$

K. RAMARAO,[1] B. RAJESH BABU [ID],[2,7] B. KISHORE BABU,[3]
V. VEERAIAH,[1] S.D. RAMARAO,[4,6] K. RAJASEKHAR,[1]
and A. VENKATESWARA RAO[5]

1.—Department of Physics, Andhra University, Visakhapatnam 530003, India. 2.—Department of Physics, GVP College of Engineering For Women, Visakhapatnam 530048, India. 3.—Department of Engineering Chemistry, AU College of Engineering, Visakhapatnam 530003, India. 4.—Department of Physics, K L University, Vaddeswaram, Guntur 522502, India. 5.—Advanced Functional Materials Research Centre, Department of Physics, Koneru Lakshmaiah Education Foundation, Vaddeswaram, Guntur, Andhra Pradesh 522502, India. 6.—New Chemistry Unit, Jawaharlal Nehru Centre for Advanced Scientific Research, Bangalore 560064, India. 7.—e-mail: rajeshbabu.bitra@gmail.com

Polycrystalline spinel ferrites Zn$_x$Mg$_{1-x}$Fe$_2$O$_4$ (where x = 0.0, 0.1, 0.15, 0.2, 0.25 and 0.3) were prepared by standard ceramic method and characterized by x-ray diffraction, Fourier transform infrared spectroscopy (FTIR), and vibrating sample magnetometer. Structural, electric and magnetic properties have been discussed in detail on the basis of Zn composition. The composition shows formation of a single-phase cubic spinel structure and the lattice constant 'a' increases with increasing Zn concentration. FTIR spectra show two prominent frequency bands in the wave number range 400–600 cm^{-1}, which further confirms the cubic spinel structure and completion of chemical reaction. Magnetic studies revealed that the saturation magnetization increases with increasing the substitution of Zn. Cation distribution for the present system was estimated by comparing observed and calculated x-ray line intensities. From this it is observed that Zn^{2+} ions prefer to occupy A sites, and Mg^{2+} and Fe^{3+} ions distributed into both A and B sites. The observed variation in magnetization has been explained on the basis of distribution of cations among A and B sites of the spinel lattice. A significant influence of cation distribution is observed on DC electrical resistivity and activation energy.

Key words: Mg-Zn ferrite, solid-state reaction, XRD, VSM, FE-SEM

INTRODUCTION

Spinel ferrites are promising ceramic magnetic materials due to their potential applications in microelectronics, microwave devices and as a core material in telecommunications at higher frequencies. The general formula of spinel ferrites can be written as AFe$_2$O$_4$ (where A is a divalent metal ion). The unit cell of spinel ferrite comprises 32 oxygen ion forming a cubic, closed-pack arrangement in which 8 are tetrahedral sites (A) and 16 are octahedral sites [B]. Studies have revealed that cations occupying A and B sites are significantly changes the electromagnetic properties of the ferrite.

Among the spinel ferrites, numerous works have been carried out on Mg–Zn ferrites due to their potential applications at high frequencies. Magnesium ferrite (MgFe$_2$O$_4$) is a soft magnet suitable for microwave devices, satellite communication, transformers, audio–video in digital recording, and as ferrite core due to the low coercivity and high resistivity.[1] Several authors studied the influence of cation distribution on the physical properties of magnesium ferrite and the distribution of cations

among A and B sites reported as $(Mg_{1-x}^{2+}Fe_x^{3+})[Mg_x^{2+}$ $Fe_{2-x}^{3+}]O_4^{2-}$, where round and square brackets denoted tetrahedral (A) and octahedral [B] sites, respectively, and x represents the degree of inversion.[2,3] However, the amount of Mg ions occupying each site is temperature-dependent. Therefore, minor changes in the distribution of cations and their occupancy ratio among A and B sited due to thermal treatment changes in electromagnetic properties. On the other hand, zinc ferrite ($ZnFe_2O_4$) has a normal spinel structure, in which the majority of Zn^{2+} ions occupy the A sites while the B sites are occupied by the Fe^{3+} ions. In spinel ferrite, the magnetic moments of the ions on (A) sites are antiparallel to those on the [B] sites due to the exchange interaction, which is known as superexchange interaction. This interaction is strongly influenced by the magnetic properties and depends on magnetic cation distribution between (A) and [B] sites. Thus, replacing Mg ions by Zn ions on the A site would enhance the physical properties of the ferrite to a great extent. With this view, in the present study, the influence of Zn doping on structural, magnetic and electric properties of $Mg_{1-x}Zn_xFe_2O_4$ (where x = 0.0, 0.1, 0.15, 0.2, 0.25 and 0.3) has been investigated.

EXPERIMENTAL DETAILS

Polycrystalline zinc-substituted magnesium ferrite $Mg_{1-x}Zn_xFe_2O_4$ with x = 0.0, 0.1, 0.15, 0.2, 0.25 and 0.3 samples were synthesized by a solid-state reaction method. High-purity, analytical-grade (A.R.) precursors of MgO (99.9% Himedia), Fe_2O_3 (99.9% Himedia) and ZnO (99.9%) were used as starting materials in desired proportions. The starting precursors were weighed as per stoichiometric proportions and mixed thoroughly in an agate mortar and pestle with acetone medium for 6 h. These mixed, metal-oxide powder materials were calcined at 900°C for 4 h and compacted into pellets by adding 5% polyvinyl alcohol (PVA) as a binder. Finally, the powder materials and pellets were sintered at 1200°C for 4 h followed by natural cooling to room temperature.

RESULTS AND DISCUSSION

Structural Analysis

Phase and Lattice Constant

The x-ray diffraction (XRD) pattern of all the compositions of the system $Mg_{1-x}Zn_xFe_2O_4$ (x = 0.0, 0.1, 0.15, 0.2, 0.25 and 0.3) is shown in Fig. 1. The diffracted peaks are identified as (111), (220), (311), (222), (440), (422) and (511) planes, which are present for all samples. These peaks closely correspond to the standard pattern for a spinel magnesium ferrite (JCPDS card no. 04-002-5442) and no extra reflections were observed. This ascertains the formation of a single phase of the spinel compound

without traces of any detectable impurities. The Rietveld refinement is a well-known and useful tool for structure determination.[4] It allows the determination of lattice parameters, atomic positions, occupation parameters, and isotropic and anisotropic temperature parameters. XRD patterns are analyzed by General Scattering Analysis Software (GSAS) using Rietveld refinement method. The Rietveld refinement of pure Mg ferrite is shown in Fig. 2. The experimental lattice parameter "a_{exp}" was calculated according to the following equation:

$$a_{exp} = d\sqrt{h^2 + k^2 + l^2} \qquad (1)$$

where d is the interplanar distance of each plane and (hkl) are Miller indices. The obtained values of "a_{exp}" are shown in Fig. 3 as a function of Zn concentration. The lattice constant of undoped Mg ferrite was found to be consistent with the reported values in the literature.[5,6] A slight enhancement in the lattice constant is observed with substitution of Zn^{2+} content. Similar behavior in the lattice constant as a function of Zn is reported in the literature.[7,8] The observed decrease in lattice constant has been attributed to the difference in the ionic radii of Mg and Zn. The substitution of the smaller-ionic-radii Zn^{2+} (0.6 Å) ions in place of large Mg^{2+} (0.72 Å) ions and their occupancy ratio in tetrahedral and octahedral sites results in a gradual increase in the lattice constant. The average crystallite size (D_{311}), cell volume (V_c), x-ray density (d_x) are calculated from XRD data and bulk density (d_b) is measured from Archimedes' method by using the following equations and the results are listed in Table I.

Crystallite size (D) is calculated by the following well-known Scherrer equation:
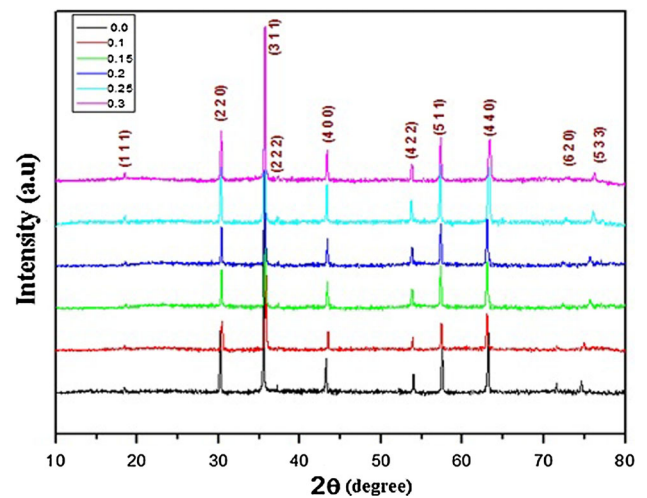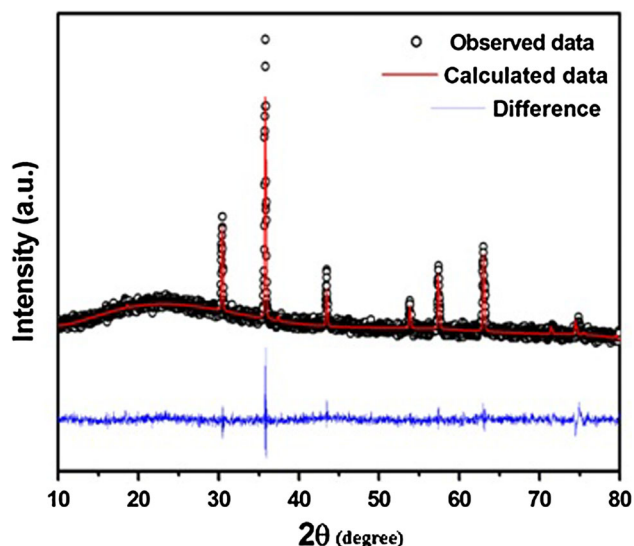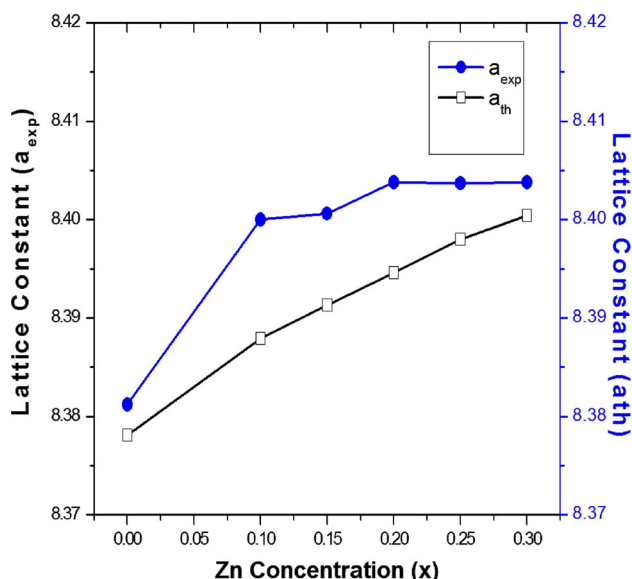
$$D_{311} = \frac{k\lambda}{\beta \cos\theta} \qquad (2)$$

Fig. 1. XRD patterns for $Mg_{1-x}Zn_xFe_2O_4$ powders.

Fig. 2. Rietveld refined XRD pattern of Mg$_{1-x}$Zn$_x$Fe$_2$O$_4$ ($x = 0$).

Fig. 3. Lattice parameters a_{exp} and a_{th} as a function of Zn concentration Mg$_{1-x}$Zn$_x$Fe$_2$O$_4$.

$$\beta = (\beta_m - \beta_s)^{1/2} \qquad (3)$$

where 'k' is the Scherrer's constant, 'λ' is the wavelength of the x-ray used (0.154 nm), 'β' is the full width at half maximum (β_m and β_s are measured peak broadening and instrumental broadening, respectively) and 'θ' is the Bragg's angle of reflection.

$$V_c = a_{exp}^3 \qquad (4)$$

$$d_x = \frac{ZM_w}{N_A V_c} \qquad (5)$$

where 'Z' is the number of formula units in a unit cell, 'M_w' is the molecular weight of the sample and 'N_A' is Avogadro's number. The calculated values of crystallite size of the Zn-doped samples are found to be in the range of 41–20.28 nm (Table I). Average crystallite size has been observed to decrease with Zn substitution. In general, factors like liberation of energy during sintering, site preference of cations, electronic configuration and bonding energy influence the growth of crystallite size. Sharifi et al.[9] reported that more heat will be liberated when Zn is introduced in the system, which in turn obstructs the crystals growth. Also, Zn^{2+} possess complete electronic configurations (3d^{10}) and have very low covalent interaction with their neighbors (ligands). This is also a pertinent reason for the observed decrease in crystallite size with increasing Zn concentration. It is clear from Table I that the cell volume (V_c) follows the same trend similar to the lattice constant (Table I). However, no significant enhancement in lattice constant and cell volume is observed due to the insignificant difference in ionic radii of Mg and Zn ions. The values of x-ray density (d_x) and bulk density are observed to follow an inverse trend with each other (Table I). The observed increase in d_x with Zn content is due to the substitution of larger-molar-mass zinc content at the expense of Mg. In general, the magnitude of the bulk density, d_b is smaller than that of the x-ray density (d_x) due to the presence of pores created during the sintering process.

Table I. Average crystallite size (D_{311}), density (d_b, d_x), volume of the cell (V_c) and porosity (P) of Mg$_{1-x}$Zn$_x$Fe$_2$O$_4$ with composition (x)

Composition (x)	Average crystallite size (nm)	Bulk density d_b (g/cm^3)	X-ray density d_x (g/cm^3)	Cell volume (Å^3)	Porosity (%)
0.0	47.1	4.44	4.53	588.08	2.0
0.1	44.56	4.47	4.57	592.7	2.1
0.15	31.14	4.3	4.61	592.8	6.7
0.2	20.28	4.32	4.65	593.5	7.1
0.25	20.3	4.31	4.7	593.5	8.2
0.3	21	4.44	4.75	593.5	6.5

Cation Distribution and Theoretical Lattice Constant

In order to understand the variation in lattice parameters, the distribution of cations among tetrahedral (A) and octahedral [B] sites is estimated using a well-known x-ray intensity calculation method reported by Burger.[10] This method is quite suitable if there is a significant difference in scattering factors between the Zn^{2+} and Mg^{2+} ions present in the lattice. The investigation of cation distribution provides a means to develop materials with desired properties which are useful for many devices.[11] The XRD intensities of various Bragg planes such as (220), (311), (400), (440) and (422) have been considered, as the intensities of these planes (hkl) are mostly sensitive to the cation distribution in A and B sites.

$$I_{hkl} = |F|^2_{hkl} P.L_p \qquad (6)$$

where I_{hkl} is the relative integrated intensity, F_{hkl} is the structure factor, P is the multiplicity factor and L_p is the Lorentz polarization factor. In the process of arriving at the final cation distribution, the site occupancy of all the cations was varied for many combinations, and those that agree well with the experimental intensity of the diffracted peaks were taken into consideration.[12] The final cation distribution thus obtained for $Mg_{1-x}Zn_xFe_2O_4$ system is given in Table II. It is observed that Zn^{2+} ions completely occupy A sites, while Mg^{2+} and Fe^{3+} ions are simultaneously distributed into both A and B sites. By using the cation distribution, lattice parameters have been evaluated theoretically form the following relation, since there is a correlation between the ionic radii of both A and B sub-lattices and the lattice parameter.

$$a_t = \frac{8}{3\sqrt{3}} \left[(r_A + r_o) + \sqrt{3}(r_B + r_o) \right] \qquad (7)$$

where r_o is the radius of the oxygen ion (0.138 nm) and r_A and r_B are the ionic radii of tetrahedral (A) and octahedral [B] sites, respectively. The values of the theoretical and experimental lattice parameters follow the same trend for all values of 'x' (Fig. 3), which confirms the agreeability of the suggested cation distribution.

Infrared Spectra

Infrared spectroscopy is an important tool to identify the functional groups, phase and purity of samples. FTIR absorption measurements were carried out using the KBr pellet technique. Figure 4 depicts the FTIR spectrum of Zn^{2+}-substituted $MgFe_2O_4$ in the range of 1000–400 cm^{-1}. It is observed that the two prominent absorption bands corresponding to the metal-oxide (M–O) stretching vibrations of tetrahedral (v_1) and octahedral (v_2) sites around 570 cm^{-1} and 400 cm^{-1}, respectively. The observed bands from FTIR spectra provide supportive evidence of the formation of a single-phase cubic spinel structure. The difference in the frequency assignment is due to the difference in the bond length between octahedral and tetrahedral coordinates. The spectra show (Fig. 4) a shifting of frequency in tetrahedral bands and no significant change in octahedral bands with increasing Zn concentration. The tetrahedral bands are shifted from a higher band value (573.84 cm^{-1}) to a lower band value (569.45 cm^{-1}). The octahedral bands are shifted from a higher band value (406.99 cm^{-1}) to a lower band value (400.02 cm^{-1}). The shifting of v_1 and v_2 reconfirms the cation distribution in both octahedral and tetrahedral sites. In general, the shift towards higher frequency can be attributed to the shifting of Fe^{+3} ions towards the O^{-2} ions.[13] The band frequencies v_1 and v_2 are reported in Table III. Besides, the octahedral band exhibits splitting of absorption bands, including a few small subsidiary bands. The detected subsidiary bands are mainly due to John–Teller distortion evolved by the presence of ferrous (Fe^{2+}) ions.[14,15] The force constant can be calculated for the tetrahedral site (K_t) and octahedral site (K_o) by using the method suggested by Waldron.[16]

$$K_t = 7.62 \times M_1 \times \vartheta_1^2 \times 10^{-3} \text{dyne/cm} \qquad (8)$$

$$K_o = 10.62 \times \frac{M_2}{2} \times \vartheta_2^2 \times 10^{-3} \text{dyne/cm} \qquad (9)$$

where M_1 and M_2 are the molecular weights of cations present at A and B sites, respectively. Both M_1 and M_2 were calculated from the cation distribution formula suggested in Table II. The

Table II. Cation distribution of $Mg_{1-x}Zn_xFe_2O_4$ with composition (x)

Co content (x)	Experimental		Calculated		A site	B site
	I_{220}/I_{400}	I_{400}/I_{422}	I_{220}/I_{400}	I_{400}/I_{422}		
0	1.1232	0.9132	1.1911	0.8612	$Mg^{2+}_{0.2} Fe^{3+}_{0.8}$	$Mg^{2+}_{0.8}Fe^{3+}_{1.2}$
0.1	1.1456	0.9258	1.1877	0.8743	$Zn^{2+}_{0.1}Mg^{+2}_{0.09} Fe^{+3}_{0.81}$	$Mg^{+2}_{0.81} Fe^{+3}_{1.19}$
0.15	1.1262	0.9049	1.3541	0.8911	$Zn^{2+}_{0.15}Mg^{+2}_{0.085} Fe^{+3}_{0.765}$	$Mg^{+2}_{0.765} Fe^{+3}_{1.235}$
0.2	1.1366	0.9041	1.1584	0.8924	$Zn^{2+}_{0.2}Mg^{+2}_{0.08} Fe^{+3}_{0.72}$	$Mg^{+2}_{0.72} Fe^{+3}_{1.28}$
0.25	1.1138	0.9237	1.1594	0.8625	$Zn^{2+}_{0.25}Mg^{+2}_{0.075} Fe^{+3}_{0.675}$	$Mg^{+2}_{0.675} Fe^{+3}_{1.325}$
0.3	1.1589	0.9162	1.2675	0.859	$Zn^{2+}_{0.3}Mg^{+2}_{0.07} Fe^{+3}_{0.67}$	$Mg^{+2}_{0.63} Fe^{+3}_{1.33}$

calculated values of the force constants K_t and K_o are listed in Table III. It can be seen that both K_t and K_o increase with increasing Zn content. Furthermore, the calculated values of K_t are greater than that of K_o, due to the A-site bond length (r_A) being smaller than the B-site bond length (r_B). The increase in force constants with increasing Zn content suggests the strengthening of interatomic bonding.

Scanning Electron Microscopy

It is well known that grain size and shape strongly influence the electrical and magnetic properties of the ferrite. The surface morphology of the samples was determined via field emission scanning electron microscopy (FE-SEM). The images of the Zn-substituted $Mg_{1-x}Zn_xFe_2O_4$ (where x = 0.0, 0.1, 0.15, 0.2, 0.25 and 0.3) are shown in Fig. 5. The micrographs clearly indicate the presence of larger grains, which are sufficiently crystalline with uneven size, and have less agglomeration due to the relatively higher sintering temperature. The average grain size for each sample was estimated using Image J4 software and listed in Table III. The overall trend of average grain size increases with 'Zn' content, consistent with densification results. It was evident that the Zn promotes grain growth.[17]

Saturation Magnetization

The room-temperature hysteresis loops of Mg–Zn spinel ferrite are shown in Fig. 6. The magnetization of the undoped Mg ferrite sample increases with applied field strength and magnetization of the

Fig. 4. Infrared spectra as a function of Zn concentration of $Mg_{1-x}Zn_xFe_2O_4$ powders.

material attains a maximum of 20.69 emu/g with an applied field strength of 19 kOe. The lower magnetization value for undoped Mg ferrite is owing to a larger concentration of non-magnetic magnesium cations occupying B sites. The obtained magnetization value of the pristine Mg ferrite is comparatively less than that of the reported value.[18] Further, magnetization increases with increasing Zn concentration and reaches a maximum value of 44.35 emu/g. The observed variation has been explained based on Neel's two-sub-lattice model. According to the Neel sub-lattices model, in spinel-type ferrites, magnetic moments of A and B sites are aligned in a direction opposite to each other. Thus, the resultant magnetic moment depends on the difference in the magnetic moments of A and B sites. The magnetic interaction between ions present at A and B sites is comparatively stronger than that of the ions residing in the same sub-lattice, i.e. A–A or B–B. The substitution of magnetic or non-magnetic ions in the spinel ferrite alters the cation distribution. If the substituted ion has different ionic radius, this causes an increase/decrease in the bond length and bond angle. This may enhance or reduce the magnetic interaction and affects the magnetic properties of the ferrite. In the present study, the non-magnetic Zn^{2+} (0 μ_B) ions replace non-magnetic Mg^{2+} (0 μ_B) ions. Therefore, one can expect no change in the magnetization with increasing Zn^{2+} content. In contrast to the above argument, saturation magnetization increases with zinc substitution. Thus, the presence of Fe^{3+} ions and their distribution is responsible for the observed variation in magnetization. In the present case, Mg^{2+} and Fe^{3+} ions are partially distributed into A and B sites in different proportions (Table II) and Zn^{2+} ions preferentially occupy tetrahedral sites (A). Due to this reason, a fraction of Fe^{3+} ions with a large magnetic moment (5 μ_B) migrates from A sites to B sites. This migration causes an increase in magnetic moment of B sites. As mentioned above, the resultant magnetic moment of the spinel lattice is the difference between magnetic moments of A and B sites. Therefore, the net magnetic moment of the system increases. The present cation distribution estimated from x-ray line intensity calculations supports the observed variation in magnetization.

It is well known that the coercivity varies inversely with the grain size. The samples with larger grain size would have greater number of domain walls. In the process of magnetization or demagnetization, the domain wall movement increases with the number of domain walls. The domain wall movement requires less energy than that required by domain rotation. Hence, samples with larger grain size are expected to have low coercivity values.

DC Electrical Resistivity

The temperature dependence of electrical resistivity (ρ) for $Mg_{1-x}Zn_xFe_2O_4$ is shown in Fig. 7. It is clear that all the samples exhibit a linear

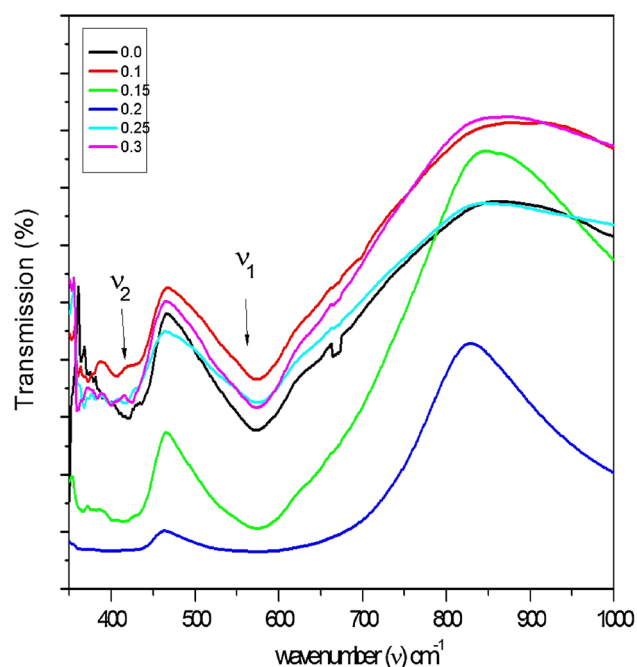**Table III. FTIR absorption band frequencies (v_1 and v_2), force constants (K_t and K_o) and average grain size of $Mg_{1-x}Zn_xFe_2O_4$ with composition (x)**

Composition (x)	v_1 (cm^{-1})	v_2 (cm^{-1})	$K_t \times 10^5$ (dyne/cm)	$K_o \times 10^5$ (dyne/cm)	Average grain size (μm)	Magnetization (emu/g)
0	573.84	406.99	1.322	0.732	1.26	20.69
0.1	572.88	401.21	1.349	0.7363	0.98	24.8
0.15	571.12	397.35	1.357	0.734	0.97	35.12
0.2	570.22	400.24	1.368	0.7569	1.42	37.76
0.25	569.45	401.12	1.38	0.772	1.04	39.65
0.3	569.45	400.02	1.427	0.77	1.53	42.43
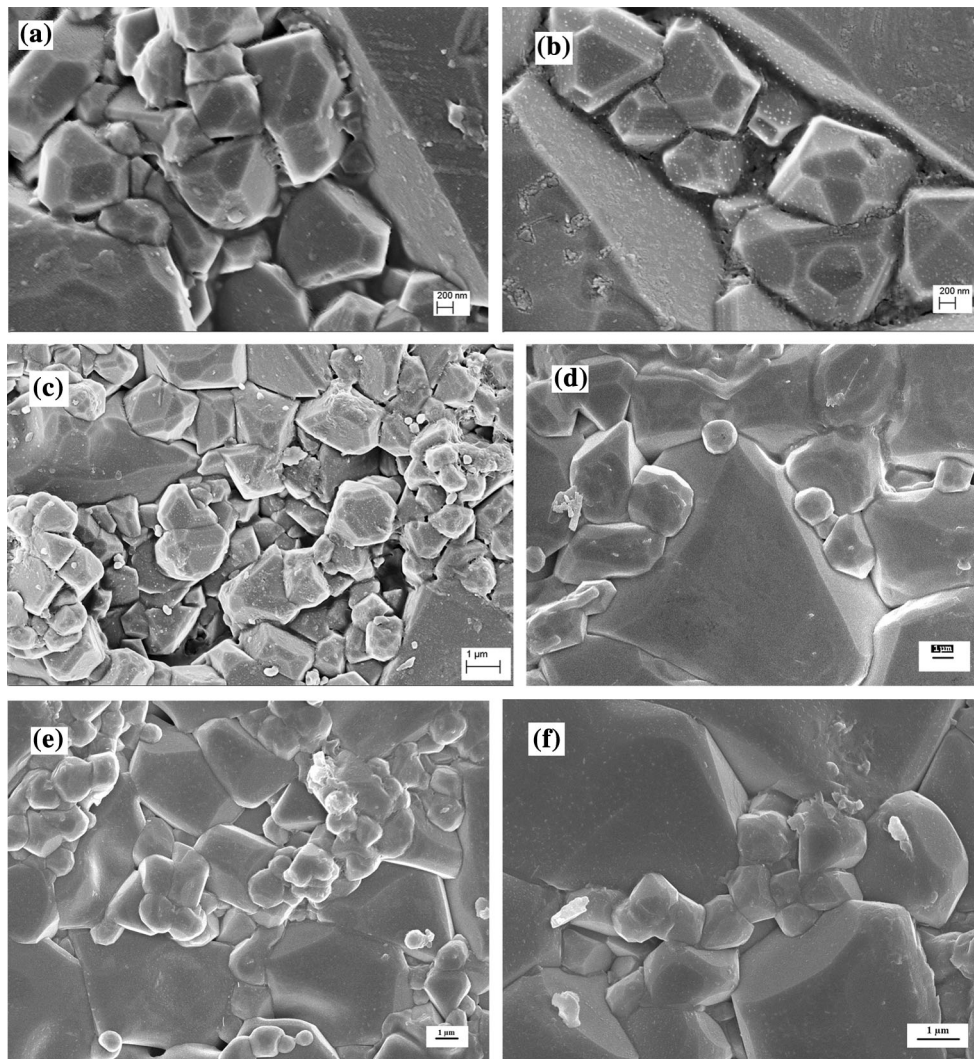
Fig. 5. FESEM images of $Mg_{1-x}Zn_xFe_2O_4$ powders (a) $x = 0.0$, (b) $x = 0.1$, (c) $x = 0.15$ (d) $x = 0.2$ (e) $x = 0.25$ and (f) $x = 0.3$.

relationship with temperature. This confirms the semiconducting nature of the prepared samples. It has been observed from Fig. 7 that resistivity decreases with increasing Zn concentration. This change in resistivity with zinc content has been explained based on the hopping mechanism. The spinel ferrites known to be low-mobility materials

and their conductivity are governed by the charge carrier transfer between the similar ions (with different valence states) presented at different octahedral sites, through a process known as "hopping mechanism".[19] Thus, hopping of electrons between Fe^{2+} and Fe^{3+} ions located on octahedral sites [B] is the primary mechanism which allows
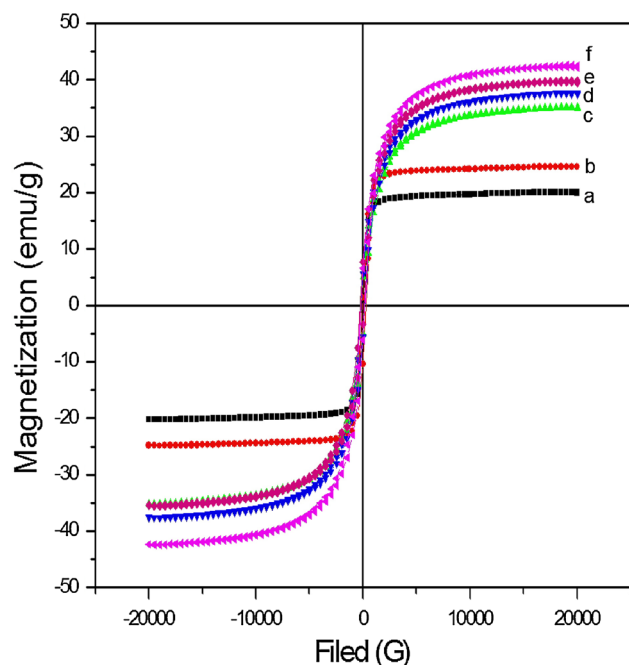
Fig. 6. Hysteresis loops of Mg$_{1-x}$Zn$_x$Fe$_2$O$_4$ (a) $x = 0$, (b) $x = 0.1$, (c) $x = 0.15$, (d) $x = 0.25$, (e) $x = 0.25$, and (f) $x = 0.3$.

Fig. 7. Temperature dependence of DC electrical resistivity of Mg$_{1-x}$Zn$_x$Fe$_2$O$_4$ powders.

electrical transport. When the samples are sintered at high temperature, the formation of oxygen vacancies causes conversion of some of the Fe^{3+} ions into Fe^{2+} ions to maintain charge neutrality of the spinel lattice. It has been reported that the presence of 0.3% Fe^{2+} content in a ferrite can reduce the electrical resistivity by a factor of more than two orders of magnitude.[20] At high sintering temperatures, zinc volatilization occurs and they escape from the samples in the form of ZnO, thus creating oxygen vacancies during the process. In this situation, to maintain charge balance, a fraction of Fe^{3+} converted into Fe^{2+} ions, resulting in increasing the hopping possibility. As the substitution of Zn increases, some Mg and Fe ions will migrate between B and A sites. From Table II, it is clear that the amount of Fe^{3+} ions at B sites increases with increasing Zn. This in turn increases the conduction at B sites, and thereby decreases the resistivity.

The electrical resistivity of ferrites also depends upon the activation energy, which is associated with the electrical energy barrier experienced by the electrons during hopping. The values of activation energy were calculated using the following relation and shown in Fig. 8 as a function of Zn concentration. The relationship between resistivity and temperature may be expressed as

$$\rho_{(T)} = \rho_o \times e^{\frac{\Delta E}{K_B T}} \qquad (10)$$

ρ_o is the pre-exponential factor with dimension of (Ω-cm), $\rho_{(T)}$ is the resistivity at T K, ΔE is the activation
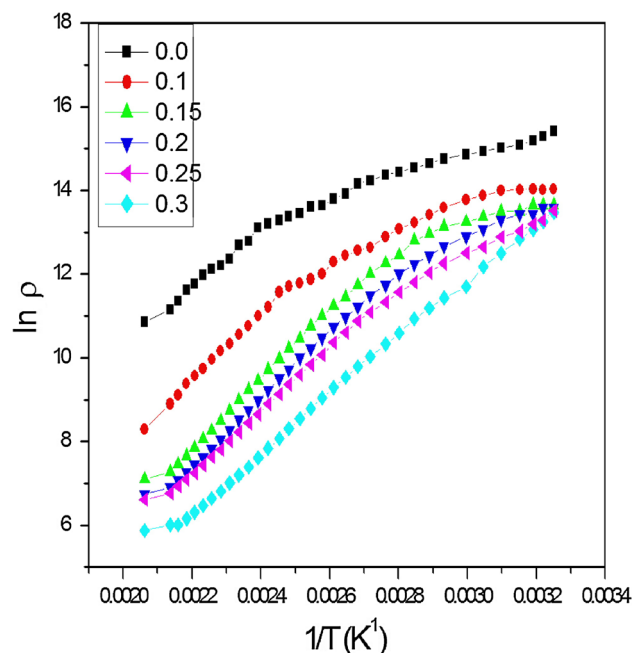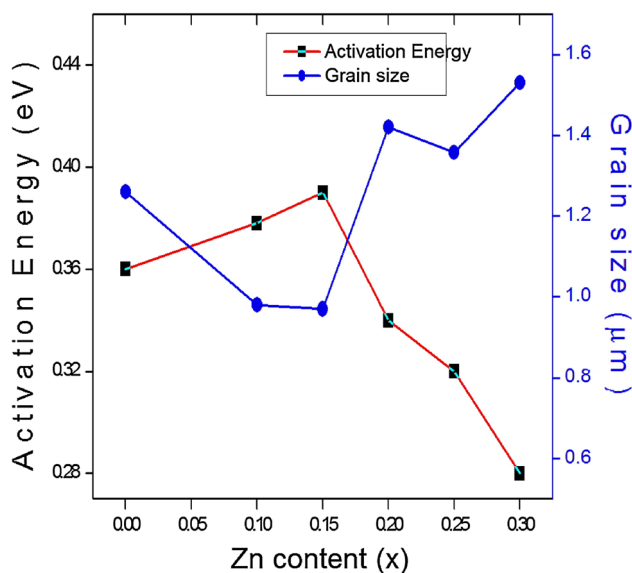

Fig. 8. Activation energy as a function of Zn content.

energy for conduction, K_B is the Boltzmann constant and T is the absolute temperature. The activation energy (ΔE) of the studied specimens was within the range 0.32–0.42 eV, which is in good agreement with previously reported values for other spinel ferrites.[21] It is well known that grain size, density and porosity strongly influence the conductivity of ferrites.[22] Figure 8 clearly shows that grain size and activation energy follow an inverse trend with each other. As discussed above, hopping of charge carriers also

varies with grain size. This is due to the fact that grain boundaries will act as poor conductors. With decreasing grain size, the number of grain boundaries also decreases, which in turn reduces the hopping of charge carriers.

CONCLUSIONS

The results of this work could be summarized as follows: Zn-doped $MgFe_2O_4$ was prepared by a solid-state sintering route. The formation of cubic spinel phase was confirmed by XRD and FTIR spectra. Structural, electrical and magnetic properties were analyzed as a function of Zn concentration. The lattice parameter decreases with increasing Zn content. Saturation magnetization follows a linear increasing trend. DC electrical resistivity and activation energy decreases, as the presence of Zn^{2+} enhances the conduction of charge carriers. It is observed that control over grain size and cation distribution is important to tailor the electric and magnetic properties.

ACKNOWLEDGEMENTS

REFERENCES

1. R.A. Mc Currie, *Ferromagnetic Materials: Structure and Properties* (London: Academic, 1994), pp. 180–234.
2. V. Sepelak, D. Baabe, F.J. Litterst, and K.D. Becker, *J. Appl. Phys.* 88, 5884 (2000).
3. S. Tao, F. Gao, X. Liu, and O.T. Sørensen, *Mater. Sci. Eng. B* 77, 172 (2000).
4. L.B. McCusker, R.B. Von Dreele, D.E. Cox, D. Louër, and P. Scardi, *J. Appl. Crystallogr.* 32, 36 (1999).
5. M.B. Henderson, J.M. Charnock, and D.A. Plant, *J. Phys. Condens. Matter* 19, 076214 (2007).
6. M. Airimioaei, M.-N. Palamaru, A.R. Iordan, P. Berthet, C. Decorse, L. Curecheriu, and L. Mitoseriu, *J. Am. Ceram. Soc.* 97, 519 (2014).
7. A. Xia, S. Liu, C. Jin, L. Chen, and L. Lv, *Mater. Lett.* 105, 199 (2013).
8. B. Rajesh Babu, B.B.V.S.V. Prasad, and M.S.R. Prasad, *Mod. Phys. Lett. B* 28, 1450244 (2014).
9. I. Sharifi and H. Shokrollahi. *J. Magn. Magn. Mat.* 324, 2397 (2012).
10. M.J. Burger, *Crystal Structure Analysis* (New York: Wiley, 1960).
11. S.M. Patange, S.E. Shirsath, B.G. Toksha, S.S. Jadhav, S.J. Shukla, and K.M. Jadhav, *Appl. Phys. A* 95, 429–434 (2009).
12. B. Rajesh Babu, K.V. Ramesh, M.S.R. Prasad, and Y. Purushotham, *J. Supercond. Nov. Magn.* 29, 939 (2016).
13. E.R. Kumar, A.S. Kamzin, and T. Prakash, *J. Magn. Magn. Mater.* 378, 389 (2015).
14. V.K. Lakhani, *Sol. State Sci.* 12, 2134 (2010).
15. L.J. Berchmens, R.K. Selvan, P.N.S. Kumar, and C.O. Augustin, *J. Magn. Magn. Mater.* 279, 103 (2004).
16. R.D. Waldron, *Phys. Rev.* 99, 1727 (1955).
17. S. Ounnunkad, P. Winotai, and S. Phanichphant, *J. Electroceram.* 16, 363 (2006).
18. A. Franco Jr. and M.S. Silva, *J. Appl. Phys.* 109, 07B505 (2011).
19. L.G. Van Uitert, *J. Chem. Phys.* 23, 1883 (1955).
20. A.M. Bhavikattia and M. Mallikarjun, Proceeding of NCRIET-2015 & *Indian J. Sci. Res.* 12, 232 (2015).
21. A.M. El-Sayed, *Mater. Chem. Phys.* 82, 583 (2003).
22. T. Methasiri, K. Yoodee, and I.M. Tang, *Phys. B* 101, 243 (1980).